

Direct Least Squares Estimation of Spatiotemporal Distributions from Dynamic Cone Beam SPECT Projections ¹

Bryan W Reutter[†], Grant T Gullberg[‡], and Ronald H Huesman[†]

[†]Center for Functional Imaging, Lawrence Berkeley National Laboratory
University of California, Berkeley, CA 94720, USA

[‡]Medical Imaging Research Laboratory, Department of Radiology
University of Utah, Salt Lake City, UT 84132, USA

Technical Report LBNL-44250

Lawrence Berkeley National Laboratory

September 13, 1999

¹This work was supported by the National Heart, Lung, and Blood Institute of the US Department of Health and Human Services under grants R01-HL50663 and P01-HL25840 and by the Director, Office of Science, Office of Biological and Environmental Research, Medical Sciences Division of the US Department of Energy under contract DE-AC03-76SF00098. This work was developed in part using the resources at the US Department of Energy National Energy Research Scientific Computing (NERSC) Center.

Disclaimer

This document was prepared as an account of work sponsored by the United States Government. While this document is believed to contain correct information, neither the United States Government nor any agency thereof, nor The Regents of the University of California, nor any of their employees, makes any warranty, express or implied, or assumes any legal responsibility for the accuracy, completeness, or usefulness of any information, apparatus, product, or process disclosed, or represents that its use would not infringe privately owned rights. Reference herein to any specific commercial product, process, or service by its trade name, trademark, manufacturer, or otherwise, does not necessarily constitute or imply its endorsement, recommendation, or favoring by the United States Government or any agency thereof, or The Regents of the University of California. The views and opinions of authors expressed herein do not necessarily state or reflect those of the United States Government or any agency thereof, or The Regents of the University of California.

Ernest Orlando Lawrence Berkeley National Laboratory is an equal opportunity employer.

Abstract

Artifacts can result when reconstructing a dynamic image sequence from inconsistent, as well as insufficient and truncated, cone beam SPECT projection data acquired by a slowly rotating gantry. The artifacts can lead to biases in kinetic model parameters estimated from time-activity curves generated by overlaying volumes of interest on the images. However, the biases in time-activity curve estimates and subsequent kinetic parameter estimates can be reduced significantly by first modeling the spatial and temporal distribution of the radiopharmaceutical throughout the projected field of view, and then estimating the time-activity curves directly from the projections. This approach is potentially useful for clinical SPECT studies involving slowly rotating gantries, particularly those using a single-detector system or body contouring orbits with a multi-detector system.

We have implemented computationally efficient methods for fully 4-D direct estimation of spatiotemporal distributions from dynamic cone beam SPECT projection data. Temporal splines were used to model the time-activity curves for the blood pool and tissue volumes in a simulated cardiac data acquisition. Least squares estimates of time-activity curves were obtained quickly and accurately using a workstation. From these curves, kinetic parameters were estimated accurately for noiseless data and with some bias for noisy data.

Keywords: dynamic SPECT, fully 4-D reconstruction, kinetic parameter estimation

1 Introduction

Conventional analysis of dynamically acquired nuclear medicine data involves fitting kinetic models to time-activity curves generated by overlaying volumes of interest on a temporal sequence of reconstructed images. Since dynamic single photon emission computed tomography (SPECT) data acquisition involves gantry motion (Figure 1) and the distribution of radiopharmaceutical changes during the acquisition (Figure 2), projections at different angles come from different tracer distributions. Images reconstructed from these inconsistent projections can contain artifacts that lead to biases in the estimated kinetic model parameters. If the SPECT data are acquired using cone beam collimators wherein the gantry rotates so that the focal point of the collimators always remains in a plane, additional biases can arise from images reconstructed using insufficient, as well as truncated, projection samples.

To overcome these problems, we and others have been investigating the estimation of time-activity curves and kinetic model parameters directly from dynamic SPECT projection data by modeling the spatial and temporal distribution of the radiopharmaceutical throughout the projected field of view [1]. This approach is potentially useful for clinical studies, particularly in those clinics which have only single-detector SPECT systems and thus are not able to perform rapid tomographic acquisitions. Even with a three-detector system, a patient study that utilizes body contouring orbits can take 45–60 sec to obtain one full tomographic acquisition. Thus, the estimation of time-activity curves and kinetic model parameters directly from projection data may also be useful for multi-detector SPECT systems acquiring data with a slowly rotating gantry.

Building on research by Carson [2] and by Formiconi [3] into direct time-activity curve estimation for regions of interest, we have used simulated volumetric data to show that unbiased kinetic parameter estimates for one-compartment models can be obtained directly from cone beam and parallel beam SPECT projections, given the blood input function and the proper segmentation of volumes encompassing the projected field of view [4,5]. We have also applied these methods to a ^{99m}Tc -teboroxime patient study for which the blood input was estimated

directly from the projections and the volumes of the left ventricular myocardium, blood pool, liver, and background tissue were determined by automatically segmenting a dynamic image sequence reconstructed from the inconsistent projection data [6]. Chiao *et al* [7,8] have jointly estimated spatial boundaries for myocardial regions of interest and kinetic parameters for one-compartment models from simulated single-slice transaxial positron emission tomography (PET) projections, using a blood input function that was estimated from the data. In addition to these methods based on segmented regions and volumes, a number of researchers have reconstructed single-slice and multi-slice parametric images from SPECT and PET data for a variety of kinetic models [9–13].

Here we present a study of the biases that result from modeling various orders of temporal continuity when estimating time-activity curves directly from dynamic cone beam and parallel beam SPECT projection data. Piecewise cubic, quadratic, linear, and constant B-splines [14] are used to model the time-activity curves for the blood input, three myocardial volumes of interest, liver, and background tissue in simulated data. Attenuation and geometric point response are modeled, but scatter is not. Segmented volumes encompassing the projected field of view are modeled to contain spatially uniform activity concentrations. Computationally efficient methods are developed which extend Formiconi's least squares algorithm [3] so that fully four-dimensional (4-D) direct spatiotemporal distribution estimation from projections can be performed on a workstation with a modest amount of memory. Using a Monte Carlo simulation, we study also the effects of noisy projections on kinetic parameter estimates for one-compartment models obtained from the spline time-activity curves for the blood input function and the myocardial and liver volumes.

The methodology presented here builds on the work of Chen *et al* [15], in which a spline fit to the blood input function and kinetic parameters for a compartmental model were jointly estimated from time-activity curves generated by overlaying regions of interest on a simulated temporal sequence of reconstructed PET images. Nichols *et al* [16] have also used splines to model the time course of activity in volume elements (voxels) reconstructed from

dynamic list mode PET data.

The methodology presented here facilitates future research into the joint estimation of the blood input function and kinetic parameters for compartmental models directly from projection data, as well as the parameterization of spatially nonuniform activity concentrations within segmented volumes encompassing the projected field of view.

2 Computationally Efficient Estimation of Spatiotemporal Distributions Directly from Projections

Time varying activity concentrations within volumes of interest encompassing the projected field of view can be modeled by selecting a set of temporal basis functions capable of representing typical time variations and having desired smoothness properties. Similarly, the spatially nonuniform activity concentration within a particular volume can be modeled by selecting an appropriate set of spatial basis functions defined within the volume. Given a set of temporal basis functions and sets of spatial basis functions for the volumes, coefficients for the resulting spatiotemporal basis functions can be estimated directly from the projections as follows.

The projection of the m^{th} spatial basis function along ray i at angle j is denoted by u_{ij}^m , and the integral of the n^{th} temporal basis function during the time interval associated with angle j of rotation k is denoted by v_{jk}^n . The projection equations can be expressed as

$$p_{ijk} = \sum_{m=1}^M \sum_{n=1}^N a_{mn} u_{ij}^m v_{jk}^n, \quad (1)$$

where M is the number of spatial basis functions and N is the number of temporal basis functions. The criterion which is minimized by varying the linear coefficients a_{mn} associated with the time integrals of the projections of the spatiotemporal basis functions is the weighted

sum of squares function

$$\chi^2 = \sum_{i=1}^I \sum_{j=1}^J \sum_{k=1}^K \frac{(p_{ijk}^* - p_{ijk})^2}{W_{ijk}}, \quad (2)$$

where the p_{ijk}^* are the measured projections, the W_{ijk} are weighting factors, I is the number of projection rays per angle, J is the number of angles per rotation, and K is the number of rotations. Typically, the weighting factors are either unity for an unweighted fit or the estimated variances of the projections for a weighted fit.

Equations (1) and (2) can be rewritten in matrix form as

$$\mathbf{p} = \mathbf{F}\mathbf{a} \quad (3)$$

and

$$\chi^2 = (\mathbf{p}^* - \mathbf{F}\mathbf{a})^T \mathbf{W} (\mathbf{p}^* - \mathbf{F}\mathbf{a}), \quad (4)$$

respectively, where \mathbf{p} is an IJK element column vector whose $[i + (j - 1)I + (k - 1)IJ]^{\text{th}}$ element is p_{ijk} , \mathbf{F} is an $IJK \times MN$ matrix whose $\{[i + (j - 1)I + (k - 1)IJ], [m + (n - 1)M]\}^{\text{th}}$ element is $u_{ij}^m v_{jk}^n$, \mathbf{a} is an MN element column vector whose $[m + (n - 1)M]^{\text{th}}$ element is a_{mn} , \mathbf{p}^* is an IJK element column vector whose $[i + (j - 1)I + (k - 1)IJ]^{\text{th}}$ element is p_{ijk}^* , and \mathbf{W} is an $IJK \times IJK$ diagonal matrix whose $[i + (j - 1)I + (k - 1)IJ]^{\text{th}}$ diagonal element is $1/W_{ijk}$. The criterion, χ^2 , is minimized by the vector of spatiotemporal basis function coefficients

$$\hat{\mathbf{a}} = (\mathbf{F}^T \mathbf{W} \mathbf{F})^{-1} \mathbf{F}^T \mathbf{W} \mathbf{p}^*. \quad (5)$$

The covariance matrix for the coefficients $\hat{\mathbf{a}}$ is

$$\text{cov}(\hat{\mathbf{a}}) = (\mathbf{F}^T \mathbf{W} \mathbf{F})^{-1} \mathbf{F}^T \mathbf{W} \text{cov}(\mathbf{p}^*) \mathbf{W} \mathbf{F} (\mathbf{F}^T \mathbf{W} \mathbf{F})^{-1}, \quad (6)$$

where $\text{cov}(\mathbf{p}^*)$ is the covariance matrix for the measured projections. Given an estimate of $\text{cov}(\mathbf{p}^*)$, estimates of the statistical uncertainties of the coefficients $\hat{\mathbf{a}}$ are the square roots of the diagonal elements of the covariance matrix given by equation (6).

Storing the entire matrix \mathbf{F} and calculating the symmetric matrix $\mathbf{F}^T \mathbf{W} \mathbf{F}$ using straightforward matrix multiplication is computationally inefficient. For example, over 3.6 million projection samples result from a 15 minute dynamic SPECT study such as that simulated in Section 3, in which data are acquired for 64 transverse \times 32 axial rays per angle ($I = 2048$), $J = 120$ angles per rotation, and one rotation per minute ($K = 15$). Fully 4-D direct spatiotemporal distribution estimation using 96 basis functions composed from $M = 6$ spatial and $N = 16$ temporal basis functions, such as are used in the simulation described in Section 3, involves a matrix \mathbf{F} containing $IJKMN \approx 350$ million elements. For an unweighted least squares reconstruction of the spatiotemporal basis function coefficients $\hat{\mathbf{a}}$ (i.e., for \mathbf{W} an identity matrix), calculating the symmetric matrix $\mathbf{F}^T \mathbf{F}$ using straightforward matrix multiplication requires $IJKMN(MN + 1)/2 \approx 17$ billion multiply-and-add operations, given \mathbf{F} . This computational burden is nontrivial for workstation-class computers and grows worse quickly as either the number M of spatial basis functions or the number N of temporal basis functions increases.

The burden of storing the matrix \mathbf{F} can be reduced significantly by storing instead the spatial basis projection factors u_{ij}^m and the temporal basis integral factors v_{jk}^n and calculating the elements of \mathbf{F} as needed. For $IJM \gg JKN$, this reduces memory usage by a factor of about KN . For the example above with $\{I, J, K, M, N\} = \{2048, 120, 15, 6, 16\}$, this requires storage of only $IJM \approx 1.5$ million u_{ij}^m factors and $JKN \approx 29$ thousand v_{jk}^n factors and reduces memory usage by a factor of about 230.

For an unweighted least squares reconstruction of the spatiotemporal basis function coefficients $\hat{\mathbf{a}}$ (i.e., for \mathbf{W} an identity matrix), the symmetric $MN \times MN$ matrix $\mathbf{F}^T \mathbf{F}$ can be calculated more efficiently as follows. Denoting the $\{[m + (n - 1)M], [m' + (n' - 1)M]\}^{\text{th}}$ element of $\mathbf{F}^T \mathbf{F}$ by $\phi^{mnm'n'}$, one has

$$\phi^{mnm'n'} = \sum_{i=1}^I \sum_{j=1}^J \sum_{k=1}^K u_{ij}^m v_{jk}^n u_{ij}^{m'} v_{jk}^{n'}. \quad (7)$$

Rearranging the summations yields

$$\phi^{mnm'n'} = \sum_{j=1}^J \left[\sum_{i=1}^I u_{ij}^m u_{ij}^{m'} \right] \left[\sum_{k=1}^K v_{jk}^n v_{jk}^{n'} \right] = \sum_{j=1}^J \mu_j^{mm'} \nu_j^{nn'}, \quad (8)$$

where $\mu_j^{mm'}$ and $\nu_j^{nn'}$ denote the inner products $\sum_{i=1}^I u_{ij}^m u_{ij}^{m'}$ and $\sum_{k=1}^K v_{jk}^n v_{jk}^{n'}$, respectively.

The number of $\mu_j^{mm'}$ factors is $JM(M+1)/2$, the number of $\nu_j^{nn'}$ factors is $JN(N+1)/2$, and the number of $\phi^{mnm'n'}$ factors is $MN(MN+1)/2$. It takes I multiply-and-add operations to calculate each $\mu_j^{mm'}$ factor and K multiply-and-add operations to calculate each $\nu_j^{nn'}$ factor. Given the $\mu_j^{mm'}$ and $\nu_j^{nn'}$ factors, it takes J multiply-and-adds to calculate each of the $\phi^{mnm'n'}$ factors. Thus, the $\phi^{mnm'n'}$ can be calculated using just $J[IM(M+1) + KN(N+1) + MN(MN+1)]/2$ multiply-and-adds. For $I \gg N^2$ and $K < M^2$, this reduces the number of operations by a factor of about KN^2 . For the example above with $\{I, J, K, M, N\} = \{2048, 120, 15, 6, 16\}$, this computationally efficient calculation of $\mathbf{F}^T \mathbf{F}$ requires storage of about 19 thousand $\mu_j^{mm'}$ and $\nu_j^{nn'}$ factors and about 6 million multiply-and-add operations, which is a factor of about 2800 less than that required for straightforward matrix multiplication. For the simulation described in Section 3, this computationally efficient calculation took about 2.2 sec.

Having addressed the major issues of storing \mathbf{F} and calculating $\mathbf{F}^T \mathbf{F}$, the next computational hurdle is calculating $\mathbf{F}^T \mathbf{p}^*$. This can be done in $(I+1)JKMN$ multiply-and-add operations, given the u_{ij}^m and v_{jk}^n factors. The system of equations $\mathbf{F}^T \mathbf{F} \hat{\mathbf{a}} = \mathbf{F}^T \mathbf{p}^*$ can then be solved efficiently for the spatiotemporal basis function coefficients $\hat{\mathbf{a}}$ using the Cholesky decomposition of $\mathbf{F}^T \mathbf{F}$ [17].

An estimate of the covariance matrix for the unweighted least squares estimates $\hat{\mathbf{a}}$ can be calculated in the following computationally efficient manner. Given an estimate $\hat{\mathbf{P}}$ of the covariance matrix for the measured projections and substituting the identity matrix for \mathbf{W} in equation (6), one obtains

$$\text{cov}(\hat{\mathbf{a}}) = (\mathbf{F}^T \mathbf{F})^{-1} \mathbf{F}^T \hat{\mathbf{P}} \mathbf{F} (\mathbf{F}^T \mathbf{F})^{-1}. \quad (9)$$

Inverting the symmetric $MN \times MN$ matrix $\mathbf{F}^T \mathbf{F}$ is straightforward, given its Cholesky decomposition. Taking the measured projections to be independent Poisson random variables, an estimate $\hat{\mathbf{P}}$ of their covariance matrix is the $IJK \times IJK$ diagonal matrix having the estimated projection vector $\hat{\mathbf{p}} = \mathbf{F}\hat{\mathbf{a}}$ along the diagonal. Denoting the $\{[m + (n - 1)M], [m' + (n' - 1)M]\}^{\text{th}}$ element of the symmetric $MN \times MN$ matrix $\mathbf{F}^T \hat{\mathbf{P}} \mathbf{F}$ by $\psi^{mnm'n'}$, one has

$$\psi^{mnm'n'} = \sum_{i=1}^I \sum_{j=1}^J \sum_{k=1}^K u_{ij}^m v_{jk}^n \hat{p}_{ijk} u_{ij}^{m'} v_{jk}^{n'}, \quad (10)$$

where \hat{p}_{ijk} is the $[i + (j - 1)I + (k - 1)IJ]^{\text{th}}$ element of the estimated projection vector $\hat{\mathbf{p}}$.

Rearranging the summations yields

$$\psi^{mnm'n'} = \sum_{j=1}^J \sum_{k=1}^K \left[\sum_{i=1}^I u_{ij}^m \hat{p}_{ijk} u_{ij}^{m'} \right] v_{jk}^n v_{jk}^{n'} = \sum_{j=1}^J \sum_{k=1}^K \omega_{jk}^{mm'} v_{jk}^n v_{jk}^{n'}, \quad (11)$$

where $\omega_{jk}^{mm'}$ denotes the weighted inner product $\sum_{i=1}^I u_{ij}^m \hat{p}_{ijk} u_{ij}^{m'}$.

The number of $\omega_{jk}^{mm'}$ factors is $JKM(M + 1)/2$ and the number of $\psi^{mnm'n'}$ factors is $MN(MN + 1)/2$. Given the \hat{p}_{ijk} , it takes $2I$ multiply operations and I add operations to calculate each $\omega_{jk}^{mm'}$ factor. Given the $\omega_{jk}^{mm'}$ factors, it takes $2JK$ multiplies and JK adds to calculate each of the $\psi^{mnm'n'}$ factors. Thus, the $\psi^{mnm'n'}$ can be calculated using just $JK[IM(M + 1) + MN(MN + 1)]$ multiply operations and half that number of add operations. Compared to the computationally efficient calculation of $\mathbf{F}^T \mathbf{F}$, this calculation of $\mathbf{F}^T \hat{\mathbf{P}} \mathbf{F}$ requires about $2K$ times more multiply-and-adds and about K times more memory, given $\hat{\mathbf{P}}$. For the case where $\hat{\mathbf{P}}$ is the diagonal matrix having the estimated projection vector $\hat{\mathbf{p}} = \mathbf{F}\hat{\mathbf{a}}$ along the diagonal, calculating $\hat{\mathbf{P}}$ takes $2IJKMN$ multiplies and half that number of adds, which is about $2N/(M + 1)$ times more operations than needed to calculate $\mathbf{F}^T \hat{\mathbf{P}} \mathbf{F}$. Thus, given a calculation time of about 2.2 sec for $\mathbf{F}^T \mathbf{F}$ and $K = 15$ rotations, such as in the simulation described in Section 3, calculation of $\mathbf{F}^T \hat{\mathbf{P}} \mathbf{F}$ should take about 1 min. For $M = 6$ spatial basis functions and $N = 16$ temporal basis functions, calculation of $\hat{\mathbf{P}}$ should take about 5 min.

For a weighted least squares reconstruction of the spatiotemporal basis function coefficients $\hat{\mathbf{a}}$ (i.e., for $\mathbf{W}^{-1} = \text{cov}(\mathbf{p}^*)$ in equations (5) and (6)), calculating $\mathbf{F}^T \mathbf{W} \mathbf{F}$ takes the

same amount of computation as calculating $\mathbf{F}^T \hat{\mathbf{P}} \mathbf{F}$. Thus, for dynamic SPECT projection data acquired with a relatively small number of rotations K , it appears that with these methods a workstation with a modest amount of memory can be used to perform a weighted least squares reconstruction of the spatiotemporal basis function coefficients $\hat{\mathbf{a}}$, as well as to obtain an estimate of the covariance matrix for the coefficients, in a reasonable amount of time. These methods are easily parallelized, and additional savings in computation can be realized by taking advantage of the sparsity of nonzero spatial basis projection factors u_{ij}^m and nonzero temporal basis integral factors v_{jk}^n .

3 Computer Simulations

The Mathematical Cardiac Torso (MCAT) phantom [18], developed by the University of North Carolina Medical Imaging Research Laboratory, was used in a simulation to evaluate the ability to estimate spatiotemporal distributions directly from dynamic cone beam and parallel beam SPECT projections using unweighted least squares. Kinetic parameters for one-compartment models (Figure 2) were estimated from the resulting spatiotemporal distributions, as well. The MCAT emission phantom (Figure 3a) contained three myocardial volumes of interest (normal myocardium, septal defect, and lateral defect), blood pool, liver, and background tissue. The myocardial defects were defined as the intersection of 3 cm diameter spheres with the septal and lateral walls of the left ventricle. Cone beam and parallel beam projections were attenuated using the corresponding MCAT attenuation phantom (Figure 3b).

The simulated time-activity curves for the six emission volumes are shown in Figure 4. The time-activity curves for the three myocardial volumes of interest and the liver were generated by using the blood pool curve as the input to one-compartment models having kinetics corresponding to those of teboroxime [19–21]. The background tissue activity was proportional to the blood pool activity.

The simulated 15 minute data acquisition consisted of 64 transverse \times 32 axial rays per angle ($I = 2048$), $J = 120$ angles per rotation, and one rotation per minute ($K = 15$) of a single-detector system. The projection bins were 7 mm \times 7 mm at the detector for both the cone beam and parallel beam geometries, and the detector was 30 cm from the center of the field of view. The collimators had a hole diameter of 2 mm, a length of 4 cm, and were offset 1 cm from the detector. The cone beam collimators had a focal length of 70 cm. Attenuation and geometric point response were modeled using a ray-driven projector with line length weighting [22]. Scatter was not modeled.

3.1 Spatiotemporal Distribution Estimates

The spatial basis functions were defined using the known segmentation of the six emission volumes composing the MCAT phantom (Figure 3a). Each emission volume was modeled to contain spatially uniform activity, which yielded $M = 6$ spatial basis functions.

The temporal basis functions consisted of $N = 16$ splines spanning 15 time segments having geometrically increasing length (Figure 5). Piecewise cubic, quadratic, linear, and constant B-splines were used with initial time segment lengths ranging between 2.5–60 sec. The shorter initial time segment lengths provided a higher density of temporal spline basis functions at the beginning of the simulated acquisition, when the activity concentrations were changing most rapidly (Figure 4). The 60 sec initial time segment length provided basis functions spaced uniformly in time. The cubic, quadratic, and linear B-splines allow modeling of curves that are continuous through their second, first, and zeroth derivative, respectively.

The computational benefits of factoring the matrix \mathbf{F} into the spatial basis projection factors u_{ij}^m and the temporal basis integral factors v_{jk}^n were evident in the simulation. Rather than storing its more than 350 million elements, about 1.5 million u_{ij}^m and v_{jk}^n factors were stored instead. The number of multiply-and-adds used to calculate $\mathbf{F}^T \mathbf{F}$ was reduced from over 17 billion to less than 6 million. A set of time-activity curves was estimated directly

from the 3.7 million simulated projection samples in about 2.3 min on a 194 MHz MIPS R10000-based Silicon Graphics workstation. The calculations of $\mathbf{F}^T \mathbf{F}$ and $\mathbf{F}^T \mathbf{p}^*$ took about 2.2 sec and 2.2 min, respectively.

Figure 6 depicts the root mean square (RMS) differences between the simulated time-activity curves and the spline curves estimated directly from noiseless projections, normalized by the RMS values of the simulated curves and expressed as percentages. The temporal spline modeling errors were largest for the septal and lateral defects, which had relatively small spatial supports (Figure 3a) and low activity concentrations (Figure 4). Intermediate errors resulted for the blood pool and background, which had larger spatial supports but quickly decaying activity concentrations. The errors were smallest for the normal myocardium and liver, which had larger spatial supports and high activity concentrations throughout the simulated data acquisition. The errors tended to increase as the length of the initial time segment for the splines increased.

In most cases the temporal spline modeling errors for the three myocardial volumes of interest and the blood pool were smaller for the cone beam geometry than for the parallel beam geometry, due to the increased relative sensitivity to those volumes provided by the cone beam sampling. Errors for the background tissue were comparable for both geometries, while in most cases the errors for the liver were larger for the cone beam geometry. For the cone beam geometry and the relatively rapid initial sampling provided by using initial time segment lengths of 2.5, 5, or 10 sec, the errors for all six volumes ranged between 0.020–3.8%, 0.022–1.7%, 0.090–6.2%, and 1.6–64% for the cubic, quadratic, linear, and constant B-splines, respectively. The corresponding ranges of errors for the parallel beam geometry were 0.020–4.9%, 0.022–2.7%, 0.089–6.8%, and 1.6–62%. For the cone beam geometry and the uniform time sampling provided by using an initial time segment length of 60 sec, the errors ranged between 0.45–50%, 0.48–53%, 0.65–60%, and 4.0–110% for the cubic, quadratic, linear, and constant B-splines, respectively. The corresponding ranges of errors for the parallel beam geometry were 0.37–69%, 0.41–73%, 0.58–83%, and 4.0–140%.

3.2 Kinetic Parameter Estimates

Of interest is how the temporal spline modeling errors bias the estimates of kinetic parameters obtained from the directly estimated time-activity curves. To study this we used the program RFIT [23–25] to fit one-compartment kinetic models to the directly estimated time-activity curves for the three myocardial volumes of interest and the liver, using the directly estimated blood pool curve as the input function. The background tissue activity was modeled to be proportional to the blood pool activity, and its amplitude was also estimated.

For the one-compartment kinetic model (Figure 2), the uptake in tissue volume m is

$$Q^m(t) = k_{21}^m \int_0^t B(\tau) e^{-k_{12}^m(t-\tau)} d\tau = k_{21}^m V^m(t), \quad (12)$$

where $B(t)$ is the blood input function, k_{21}^m is the uptake parameter, and k_{12}^m is the washout parameter. Total activity in the tissue is given by

$$Q^m(t) + f_v^m B(t) = k_{21}^m V^m(t) + f_v^m B(t), \quad (13)$$

where f_v^m is the fraction of vasculature in the tissue. To fit one-compartment models for the normal myocardium, septal defect, lateral defect, and liver (denoted by indices $m = 1, 2, 3$, and 4 , respectively), RFIT varies the parameters k_{21}^m , k_{12}^m , and f_v^m to minimize the unweighted sum of squares function

$$\chi_m^2 = \sum_{j=1}^J \sum_{k=1}^K \left\{ \sum_{n=1}^N \hat{a}_{mn} v_{jk}^n - \int_{t_{jk}-\Delta t}^{t_{jk}} [k_{21}^m \hat{V}^m(\tau) + f_v^m \hat{B}(\tau)] d\tau \right\}^2, \quad (14)$$

where the \hat{a}_{mn} are given by equation (5), v_{jk}^n is the integral of the n^{th} temporal basis function during the time interval $[t_{jk} - \Delta t, t_{jk}]$ in which projection data are acquired at angle j of rotation k , $\hat{V}^m(\tau)$ is the convolution $\int_0^\tau \hat{B}(\tau') e^{-k_{12}^m(\tau-\tau')} d\tau'$, and $\hat{B}(\tau)$ is derived from the directly estimated blood pool time-activity curve (denoted by index $m = 6$) as follows. Given the set of time integrals, $\{\sum_{n=1}^N \hat{a}_{6n} v_{jk}^n; j = 1, \dots, J; k = 1, \dots, K\}$, of the directly estimated blood pool curve, RFIT models $\hat{B}(\tau)$ as a piecewise linear function which interpolates zero at time $\tau = 0$; the value $\sum_{n=1}^N \hat{a}_{6n} v_{jk}^n / \Delta t$ at time $t_{jk} - (\Delta t/2)$, for $j = 1, \dots, J$ and $k = 1, \dots, K$; and the value $\sum_{n=1}^N \hat{a}_{6n} v_{JK}^n / \Delta t$ at time t_{JK} .

The amplitude, g , of the background tissue (denoted by index $m = 5$) is estimated by minimizing the unweighted sum of squares function

$$\chi_5^2 = \sum_{j=1}^J \sum_{k=1}^K \left\{ \sum_{n=1}^N \hat{a}_{5n} v_{jk}^n - \int_{t_{jk}-\Delta t}^{t_{jk}} g \hat{B}(\tau) d\tau \right\}^2. \quad (15)$$

Figures 7, 8, and 9 show the kinetic parameter estimates obtained from the spline models for time-activity curves estimated directly from noiseless projections. The biases in the uptake parameters k_{21}^m and the washout parameters k_{12}^m were particularly small when using quadratic B-splines and initial time segment lengths of 2.5, 5, or 10 sec (Figures 7b and 8b). For these three sets of basis functions, the biases ranged between 0.0–1.0% for the cone beam geometry and 0.0–1.4% for the parallel beam geometry.

To study the effects of noisy projections on kinetic parameter estimates obtained from spline time-activity curves, 100 realizations of projections having Poisson noise were generated for both the cone beam and parallel beam geometries. The amplitude of the simulated blood input function was adjusted so that about 10 million events were detected using the cone beam collimators. With this same blood input function, about 6.4 million events were detected using the parallel beam collimators. Quadratic B-splines and an initial time segment length of 10 sec were used to model the time-activity curves. A two-tailed t test [26] was used to assess the biases in the sample means of the kinetic parameter estimates.

Figures 10, 11, and 12 show the time-activity curves estimated for the blood pool and the three myocardial volumes of interest, for the first three noisy realizations. For both the cone beam and parallel beam geometries, the differences between the spline time-activity curves estimated directly from noiseless and noisy projections are relatively small, for the blood pool and the normal myocardium. For the septal and lateral defects, the differences between the spline curves estimated directly from noiseless and noisy projections are relatively large. Noise in the spline curve coefficients generates extended excursions (dotted lines) above and below the noiseless spline curves (solid lines). The curves associated with the one-compartment kinetic model fits to the noisy spline curves provide smoother approximations

(dashed lines) to the noiseless spline curves. In all cases, the noiseless spline curves provide relatively good fits to the samples of the simulated curves.

Summaries of the results for all 100 noisy realizations are presented in Tables 1 and 2, for both the cone beam and parallel beam geometries. For the cone beam geometry (Table 1), the sample means (column (f)) of the uptake parameters k_{21}^m and the washout parameters k_{12}^m for the normal myocardium and the liver did not differ significantly from the simulated values ($P > 0.4$). The sample standard deviations (column (g)) ranged between 0.5–20%. The sample means of the uptake and washout parameters for the septal and lateral defects were significantly different from the simulated values ($P < 0.05$). The differences between the sample means and the simulated values for the defects ranged between 4.8–16%. The sample standard deviations ranged between 22–42%.

For the parallel beam geometry (Table 2), the sample means (column (f)) of the uptake parameters k_{21}^m for the normal myocardium and the liver did not differ significantly from the simulated values ($P > 0.05$). The sample means of the washout parameters k_{12}^m were significantly different from the simulated values ($P < 0.03$), although the difference was only 0.7% for the normal myocardium. The difference for the liver washout was 10%. The sample standard deviations (column (g)) ranged between 0.9–40%. The sample means of the uptake and washout parameters for the septal and lateral defects were significantly different from the simulated values ($P < 0.03$). The differences between the sample means and the simulated values for the defects ranged between 11–39%. The sample standard deviations ranged between 40–140%.

4 Discussion

The combination of gantry motion and the time-variation of the radiopharmaceutical distribution being imaged results in inconsistent dynamic SPECT projection data sets. In addition, the use of cone beam collimators can result in insufficient, as well as truncated, pro-

jection samples. Conventional kinetic model parameter estimation from time-activity curves generated by overlaying volumes of interest on images reconstructed from these projection data results in biases. The biases in the time-activity curve estimates and the subsequent kinetic model parameter estimates can be reduced significantly by estimating the time-activity curves directly from the projections. Implementation of this strategy requires a spatial and temporal model of the radiopharmaceutical distribution throughout the projected field of view.

Computational issues associated with fully 4-D direct estimation of spatiotemporal distributions from dynamic cone beam SPECT projection data have been addressed, so that least squares estimates of time-activity curves can be obtained quickly and accurately using a workstation with a modest amount of memory. Temporal B-splines were used to model the time-activity curves for the blood pool and tissue volumes in a simulated cardiac data acquisition. From these curves, kinetic parameters for compartmental models were estimated accurately for noiseless data and with some bias for noisy data.

The estimation of time-activity curves and kinetic model parameters directly from projection data is potentially useful for clinical SPECT studies involving slowly rotating gantries, particularly those which use a single-detector system or body contouring orbits with a multi-detector system. The methodology presented here facilitates future research into the joint estimation of the blood input function and kinetic parameters for compartmental models directly from projection data, as well as the parameterization of spatially nonuniform activity concentrations within segmented volumes encompassing the projected field of view.

5 Acknowledgments

We thank Dr. GL Zeng for his helpful advice, and the University of North Carolina Medical Imaging Research Laboratory for making the MCAT phantom available.

This work was supported by the National Heart, Lung, and Blood Institute of the US

Department of Health and Human Services under grants R01-HL50663 and P01-HL25840 and by the Director, Office of Science, Office of Biological and Environmental Research, Medical Sciences Division of the US Department of Energy under contract DE-AC03-76SF00098. This work was developed in part using the resources at the US Department of Energy National Energy Research Scientific Computing (NERSC) Center.

References

- [1] Gullberg GT, RH Huesman, SG Ross, EVR Di Bella, GL Zeng, BW Reutter, PE Christian, and SA Foresti. Dynamic cardiac single-photon emission computed tomography. In Zaret BL and GA Beller, editors, *Nuclear Cardiology: State of the Art and Future Directions*, chapter 11, pages 137–187. Mosby Inc, St Louis, 1999.
- [2] Carson RE. A maximum likelihood method for region-of-interest evaluation in emission tomography. *J Comput Assist Tomogr*, **10**(4):654–663, 1986.
- [3] Formiconi AR. Least squares algorithm for region-of-interest evaluation in emission tomography. *IEEE Trans Med Imag*, **12**(1):90–100, 1993.
- [4] Huesman RH, BW Reutter, GL Zeng, and GT Gullberg. Kinetic parameter estimation from SPECT cone-beam projection measurements. *Phys Med Biol*, **43**(4):973–982, 1998.
- [5] Reutter BW, GT Gullberg, and RH Huesman. Kinetic parameter estimation from attenuated SPECT projection measurements. *IEEE Trans Nucl Sci*, **45**(6):3007–3013, 1998.
- [6] Reutter BW, GT Gullberg, and RH Huesman. Kinetic parameter estimation from dynamic cardiac patient SPECT projection measurements. In Sudharsanan R, editor, *1998 IEEE Nuclear Science Symposium and Medical Imaging Conference Record*, pages 1953–1958, 1999.

- [7] Chiao PC, WL Rogers, NH Clinthorne, JA Fessler, and AO Hero. Model-based estimation for dynamic cardiac studies using ECT. *IEEE Trans Med Imag*, **13**(2):217–226, 1994.
- [8] Chiao PC, WL Rogers, JA Fessler, NH Clinthorne, and AO Hero. Model-based estimation with boundary side information or boundary regularization. *IEEE Trans Med Imag*, **13**(2):227–234, 1994.
- [9] Carson RE. *Two Image-Wide Parameter Estimation Methods for Positron Emission Tomography: Theory and Application to the Measurement of Local Cerebral Blood Flow in Humans*. PhD thesis, University of California, Los Angeles, 1983.
- [10] Snyder DL. Parameter estimation for dynamic studies in emission-tomography systems having list-mode data. *IEEE Trans Nucl Sci*, **31**(2):925–931, 1984.
- [11] O’Sullivan F. Imaging radiotracer model parameters in PET: A mixture analysis approach. *IEEE Trans Med Imag*, **12**(3):399–412, 1993.
- [12] Meikle SR, JC Matthews, VJ Cunningham, DL Bailey, L Livieratos, T Jones, and P Price. Parametric image reconstruction using spectral analysis of PET projection data. *Phys Med Biol*, **43**(3):651–666, 1998.
- [13] Bauschke HH, D Noll, A Celler, and JM Borwein. An EM algorithm for dynamic SPECT. *IEEE Trans Med Imag*, **18**(3):252–261, 1999.
- [14] Bartels RH, JC Beatty, and BA Barsky. *An Introduction to Splines for Use in Computer Graphics and Geometric Modeling*. M Kaufmann Publishers, Los Altos, California, 1987.
- [15] Chen K, SC Huang, and DC Yu. The effects of measurement errors in the plasma radioactivity curve on parameter estimation in positron emission tomography. *Phys Med Biol*, **36**(9):1183–1200, 1991.

- [16] Nichols TE, J Qi, and RM Leahy. Continuous time dynamic PET imaging using list mode data. In *Information Processing in Medical Imaging: Proceedings of the Sixteenth International Conference*, pages 98–111, 1999.
- [17] Press WH, SA Teukolsky, WT Vetterling, and BP Flannery. *Numerical Recipes in Fortran 90: The Art of Parallel Scientific Computing*. Cambridge University Press, Cambridge, England, 1996.
- [18] Tsui BMW, JA Terry, and GT Gullberg. Evaluation of cardiac cone-beam single photon emission computed tomography using observer performance experiments and receiver operating characteristic analysis. *Invest Radiol*, **28**(12):1101–12, 1993.
- [19] Narra RK, T Feld, and AD Nunn. Absorbed radiation dose to humans from technetium-99m-teboroxime. *J Nucl Med*, **33**(1):88–93, 1992.
- [20] Smith AM, GT Gullberg, PE Christian, and FL Datz. Kinetic modeling of teboroxime using dynamic SPECT imaging of a canine model. *J Nucl Med*, **35**(3):984–995, 1994.
- [21] Smith AM, GT Gullberg, and PE Christian. Experimental verification of ^{99m}Tc -teboroxime kinetic parameters in the myocardium using dynamic SPECT: Reproducibility, correlations to flow, and susceptibility to extravascular contamination. *J Nucl Cardiol*, **3**:130–142, 1996.
- [22] Zeng GL, GT Gullberg, BMW Tsui, and JA Terry. Three-dimensional iterative reconstruction algorithms with attenuation and geometric point response correction. *IEEE Trans Nucl Sci*, **38**(2):693–702, 1991.
- [23] Mazoyer BM, RH Huesman, TF Budinger, and BL Knittel. Dynamic PET data analysis. *J Comput Assist Tomogr*, **10**(4):645–653, 1986.

- [24] Coxson PG, EM Salmeron, RH Huesman, and BM Mazoyer. Simulation of compartmental models for kinetic data from a positron emission tomograph. *Comput Methods Programs Biomed*, **37**:205–214, 1992.
- [25] Huesman RH, BL Knittel, BM Mazoyer, PG Coxson, EM Salmeron, GJ Klein, BW Reutter, and TF Budinger. Notes on RFIT: A program for fitting compartmental models to region-of-interest dynamic emission tomographic data. Report LBL-37621, Lawrence Berkeley Laboratory, 1993.
- [26] DeGroot MH. *Probability and Statistics*. Addison Wesley, Reading, Massachusetts, second edition, 1986.

		cone beam						
		simulated	noiseless	noisy fits ($n = 100$)			sample	sample
		(a)	fit (b)	1 st (c)	2 nd (d)	3 rd (e)	mean (f)	std dev (g)
normal myocardium	k_{21}^1	0.700	0.700	0.697	0.697	0.707	0.700	0.0064
	k_{12}^1	0.150	0.150	0.151	0.152	0.152	0.150	0.0016
	f_v^1	0.150	0.150	0.149	0.130	0.144	0.150	0.011
septal defect	k_{21}^2	0.300	0.300	0.299	0.393	0.266	0.314*	0.072
	k_{12}^2	0.300	0.300	0.307	0.361	0.249	0.317*	0.066
	f_v^2	0.100	0.102	0.139	0.015	-0.062	0.095	0.12
lateral defect	k_{21}^3	0.500	0.502	0.628	0.569	0.713	0.578*	0.21
	k_{12}^3	0.600	0.603	0.727	0.595	0.802	0.653*	0.16
	f_v^3	0.100	0.096	0.246	-0.044	-0.034	0.064*	0.17
liver	k_{21}^4	0.900	0.900	0.901	0.893	0.903	0.900	0.0046
	k_{12}^4	0.0020	0.0020	0.0029	0.0025	0.0026	0.0020	0.0004
	f_v^4	0.200	0.201	0.197	0.196	0.191	0.201	0.0047
background	g	0.200	0.200	0.199	0.197	0.200	0.200	0.0010

Table 1: One-compartment kinetic model parameters (Figure 2) obtained from time-activity curves estimated directly from cone beam projections using temporal quadratic B-spline basis functions and an initial time segment length of 10 sec (Figure 5b): (a) simulated kinetic parameter values; (b) values from noiseless projections; (c), (d), and (e) values from the first three of 100 realizations of projections having Poisson noise (Figures 10, 11, and 12); (f) sample means for the 100 noisy realizations; (g) sample standard deviations for the 100 noisy realizations. Units for uptake k_{21}^m and washout k_{12}^m are min^{-1} . The vascular fraction f_v^m and background amplitude g are dimensionless. Sample means that were significantly different from the simulated values (i.e., $P < 0.05$ for a two-tailed t test) are labeled with asterisks. Using the cone beam collimators, about 10 million events were detected for each noisy realization.

		parallel beam						
		simulated	noiseless	noisy fits ($n = 100$)			sample	sample
			fit	1 st	2 nd	3 rd	mean	std dev
		(a)	(b)	(c)	(d)	(e)	(f)	(g)
normal myocardium	k_{21}^1	0.700	0.700	0.698	0.680	0.693	0.702	0.010
	k_{12}^1	0.150	0.150	0.148	0.149	0.148	0.151*	0.0031
	f_v^1	0.150	0.151	0.148	0.188	0.199	0.149	0.025
septal defect	k_{21}^2	0.300	0.301	0.322	0.278	0.361	0.337*	0.16
	k_{12}^2	0.300	0.301	0.397	0.257	0.413	0.333*	0.12
	f_v^2	0.100	0.100	-0.094	0.202	-0.111	0.086	0.24
lateral defect	k_{21}^3	0.500	0.507	1.102	0.783	0.707	0.694*	0.68
	k_{12}^3	0.600	0.607	0.954	0.626	0.601	0.692*	0.40
	f_v^3	0.100	0.092	-0.276	-0.435	-0.222	0.059	0.33
liver	k_{21}^4	0.900	0.900	0.894	0.893	0.904	0.901	0.0082
	k_{12}^4	0.0020	0.0020	0.0014	0.0023	0.0016	0.0022*	0.0008
	f_v^4	0.200	0.201	0.198	0.209	0.205	0.201	0.0081
background	g	0.200	0.200	0.198	0.199	0.202	0.200	0.0019

Table 2: One-compartment kinetic model parameters (Figure 2) obtained from time-activity curves estimated directly from parallel beam projections using temporal quadratic B-spline basis functions and an initial time segment length of 10 sec (Figure 5b): (a) simulated kinetic parameter values; (b) values from noiseless projections; (c), (d), and (e) values from the first three of 100 realizations of projections having Poisson noise (Figures 10, 11, and 12); (f) sample means for the 100 noisy realizations; (g) sample standard deviations for the 100 noisy realizations. Units for uptake k_{21}^m and washout k_{12}^m are min^{-1} . The vascular fraction f_v^m and background amplitude g are dimensionless. Sample means that were significantly different from the simulated values (i.e., $P < 0.05$ for a two-tailed t test) are labeled with asterisks. Using the parallel beam collimators, about 6.4 million events were detected for each noisy realization.

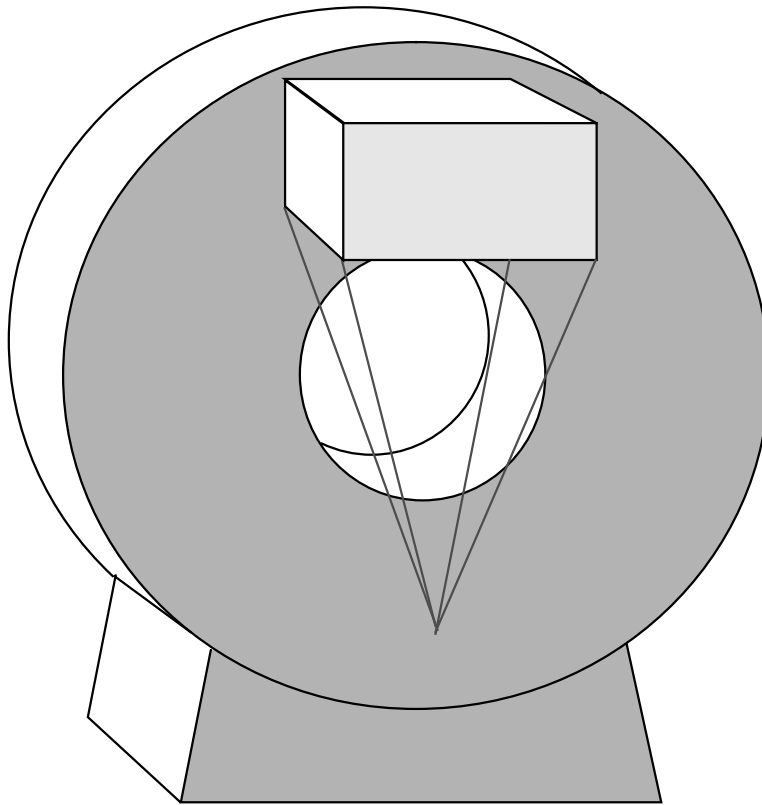


Figure 1: Cone beam SPECT scanner. The detector rotates about the patient (not shown) so that the focal point remains in a plane perpendicular to the long axis of the patient's body.

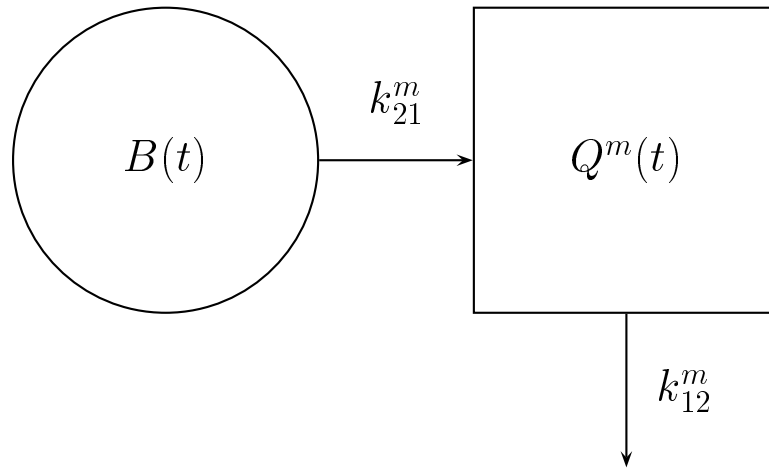
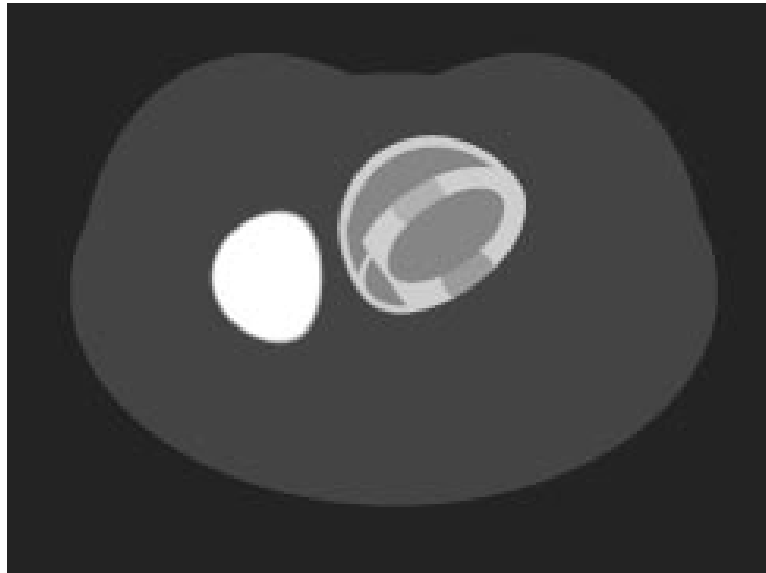


Figure 2: Compartmental model for ^{99m}Tc -teboroxime in the myocardium. $B(t)$ is the blood input function, $Q^m(t)$ is the tracer in tissue volume m , and k_{21}^m and k_{12}^m are the rate constants for uptake and washout, respectively.



(a) MCAT emission phantom.



(b) MCAT attenuation phantom.

Figure 3: Transverse cross sections through (a) the MCAT emission phantom and (b) the MCAT attenuation phantom.

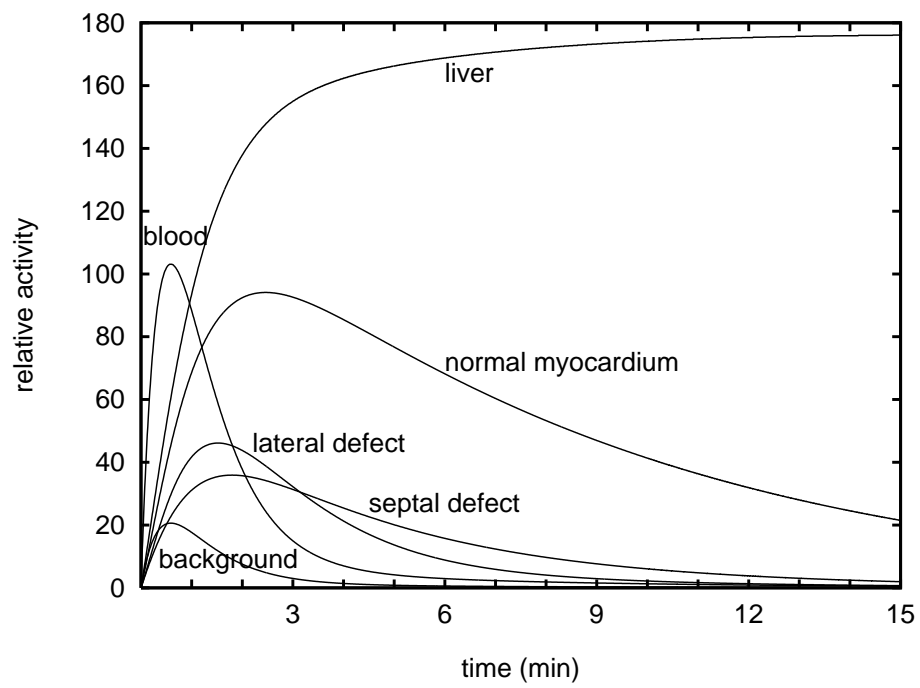
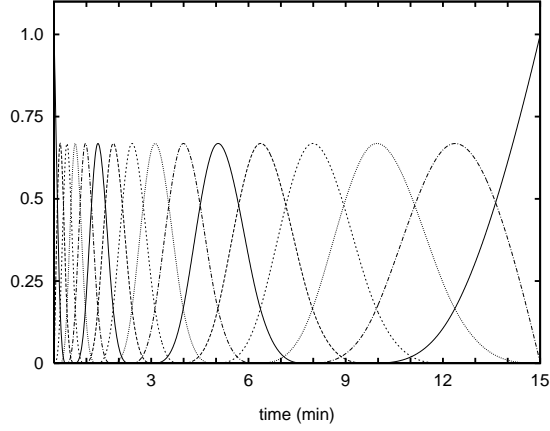
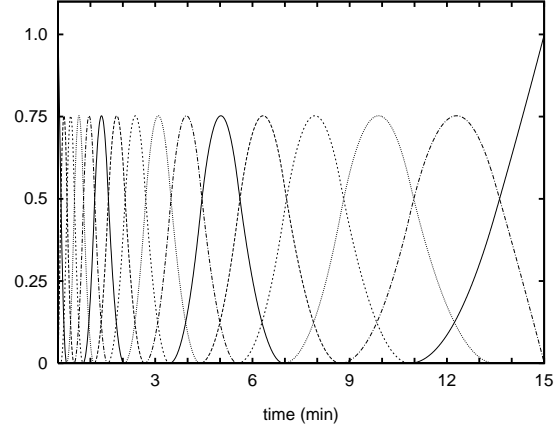


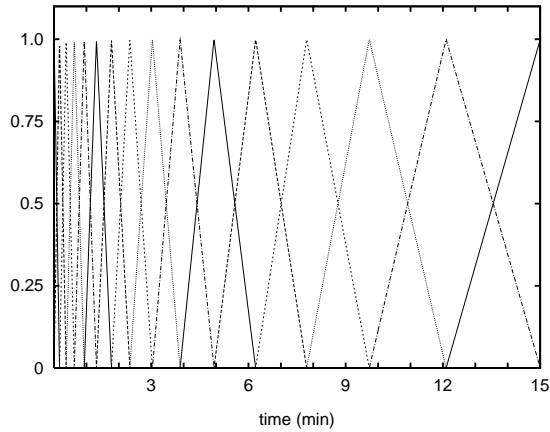
Figure 4: Simulated time-activity curves for the volumes shown in Figure 3a.



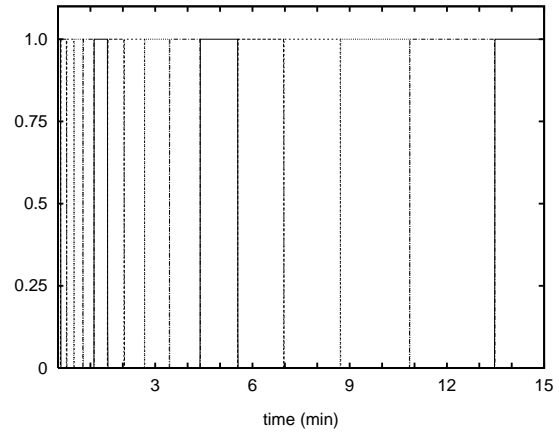
(a) Cubic B-spline temporal basis functions.



(b) Quadratic B-spline temporal basis functions.



(c) Linear B-spline temporal basis functions.



(d) Constant B-spline temporal basis functions.

Figure 5: Examples of piecewise cubic (a), quadratic (b), linear (c), and constant (d) B-spline temporal basis functions used to model time-activity curves estimated directly from projections. Sixteen splines (shown with various line patterns) were used to span 15 time segments having geometrically increasing length. The initial time segment length for the splines shown here is 10 sec, and the subsequent 14 time segments have lengths of about 12 sec, 15 sec, 18 sec, 23 sec, 28 sec, 34 sec, 42 sec, 51 sec, 1.0 min, 1.3 min, 1.6 min, 1.9 min, 2.4 min, and 2.9 min. The splines sum to one at each time point. The cubic, quadratic, and linear B-splines allow modeling of curves that are continuous through their second, first, and zeroth derivative, respectively.

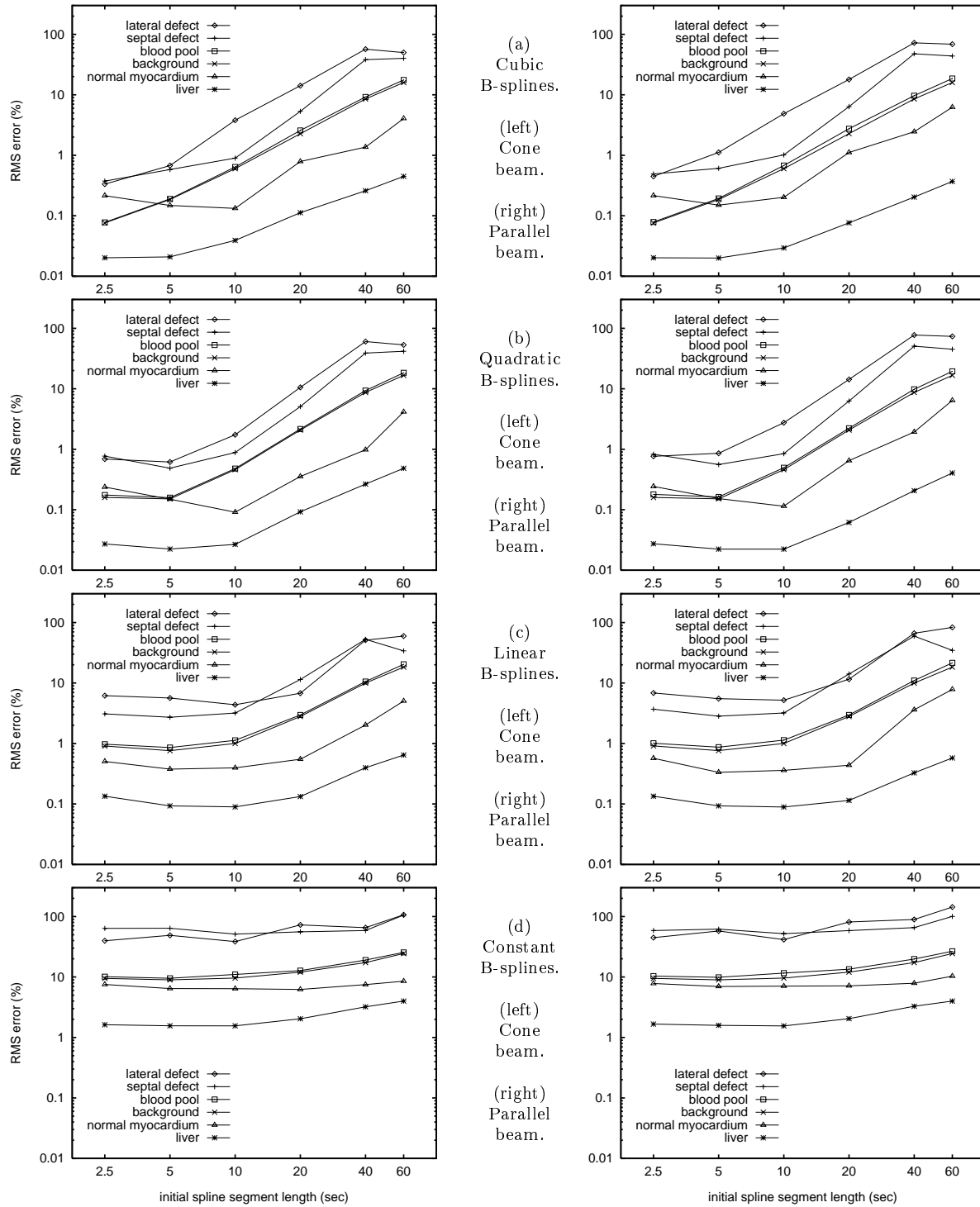


Figure 6: Root mean square (RMS) errors for time-activity curves estimated directly from simulated noiseless cone beam (left) and parallel beam (right) projections, using piecewise cubic (a), quadratic (b), linear (c), and constant (d) B-spline temporal basis functions (Figure 5) and initial time segment lengths ranging between 2.5–60 sec. The differences between the simulated time-activity curves (Figure 4) and the spline curves estimated directly from noiseless projections (e.g., the solid curves in Figure 10) are normalized by the RMS values of the simulated curves and expressed as percentages. The errors tend to increase as the length of the initial time segment for the splines increases.

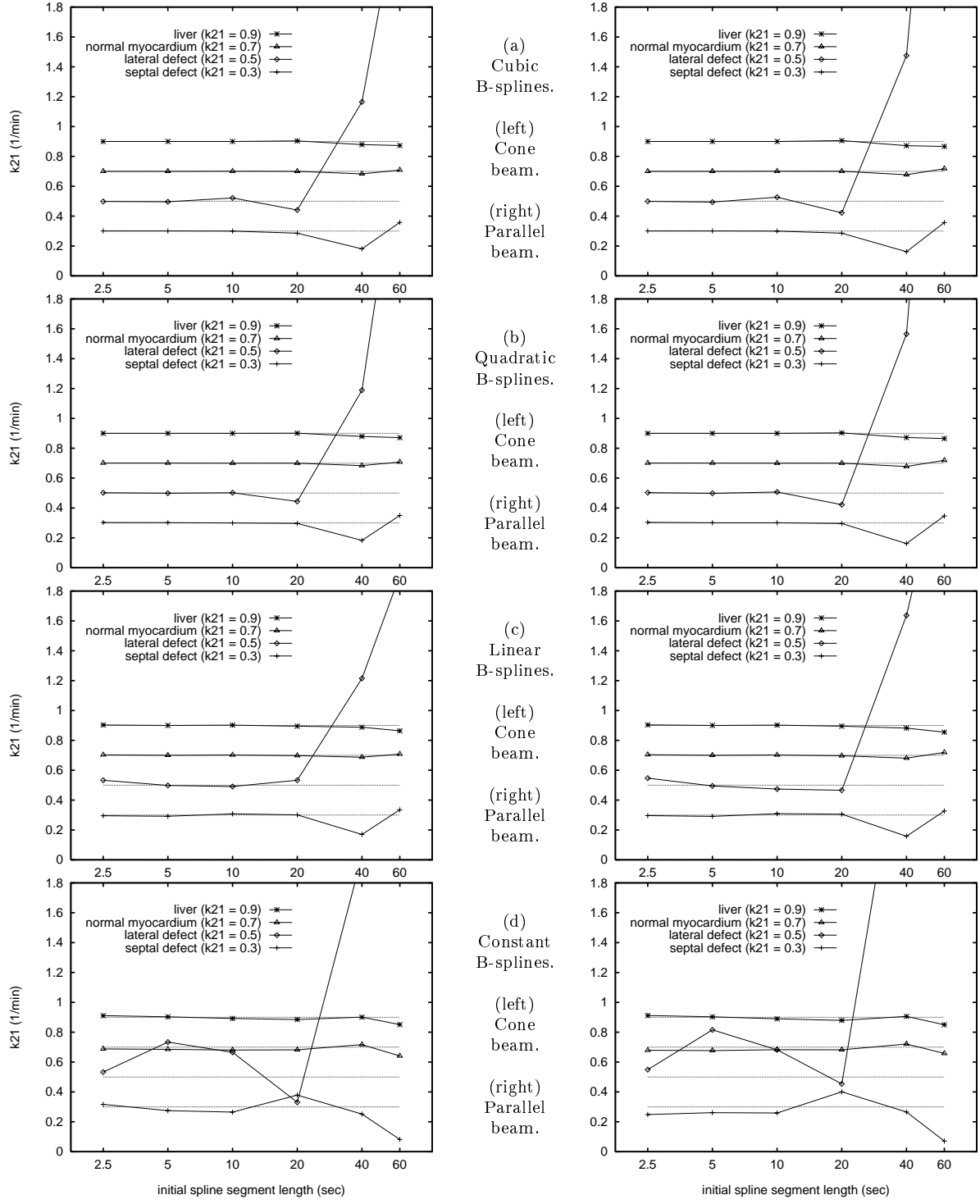


Figure 7: Uptake parameters k_{21}^m (Figure 2) obtained from time-activity curves estimated directly from simulated noiseless cone beam (left) and parallel beam (right) projections, using piecewise cubic (a), quadratic (b), linear (c), and constant (d) B-spline temporal basis functions (Figure 5) and initial time segment lengths ranging between 2.5–60 sec. Units for uptake k_{21}^m are min^{-1} . The simulated values are depicted by the dotted horizontal lines and listed in the figure legends. The biases are particularly small when using quadratic B-splines and initial time segment lengths of 2.5, 5, or 10 sec. The results for quadratic B-splines and an initial time segment length of 10 sec are listed in column (b) of Tables 1 and 2.

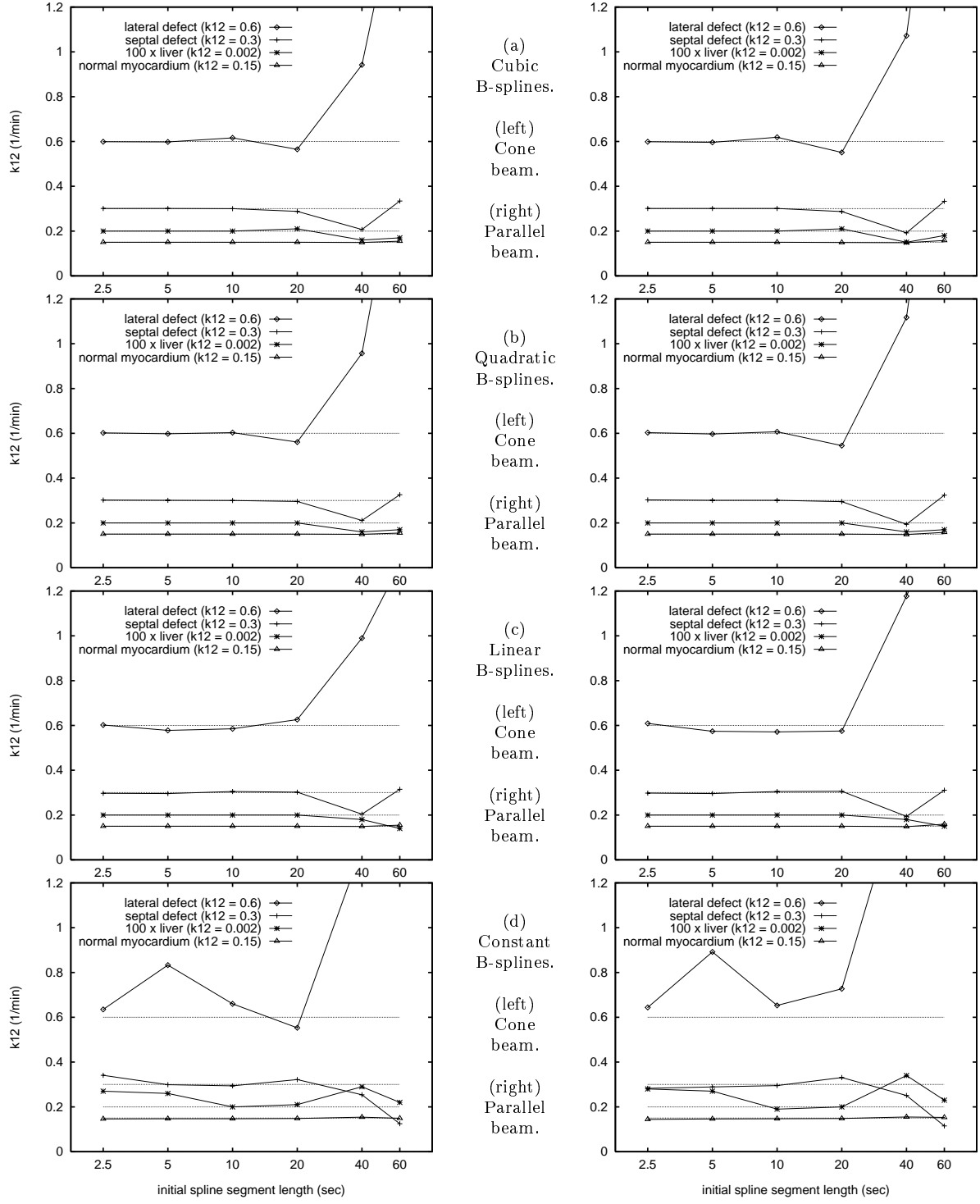


Figure 8: Washout parameters k_{12}^m (Figure 2) obtained from time-activity curves estimated directly from simulated noiseless cone beam (left) and parallel beam (right) projections, using piecewise cubic (a), quadratic (b), linear (c), and constant (d) B-spline temporal basis functions (Figure 5) and initial time segment lengths ranging between 2.5–60 sec. Units for washout k_{12}^m are min^{-1} . The simulated values are depicted by the dotted horizontal lines and listed in the figure legends. The biases are particularly small when using quadratic B-splines and initial time segment lengths of 2.5, 5, or 10 sec. The results for quadratic B-splines and an initial time segment length of 10 sec are listed in column (b) of Tables 1 and 2.

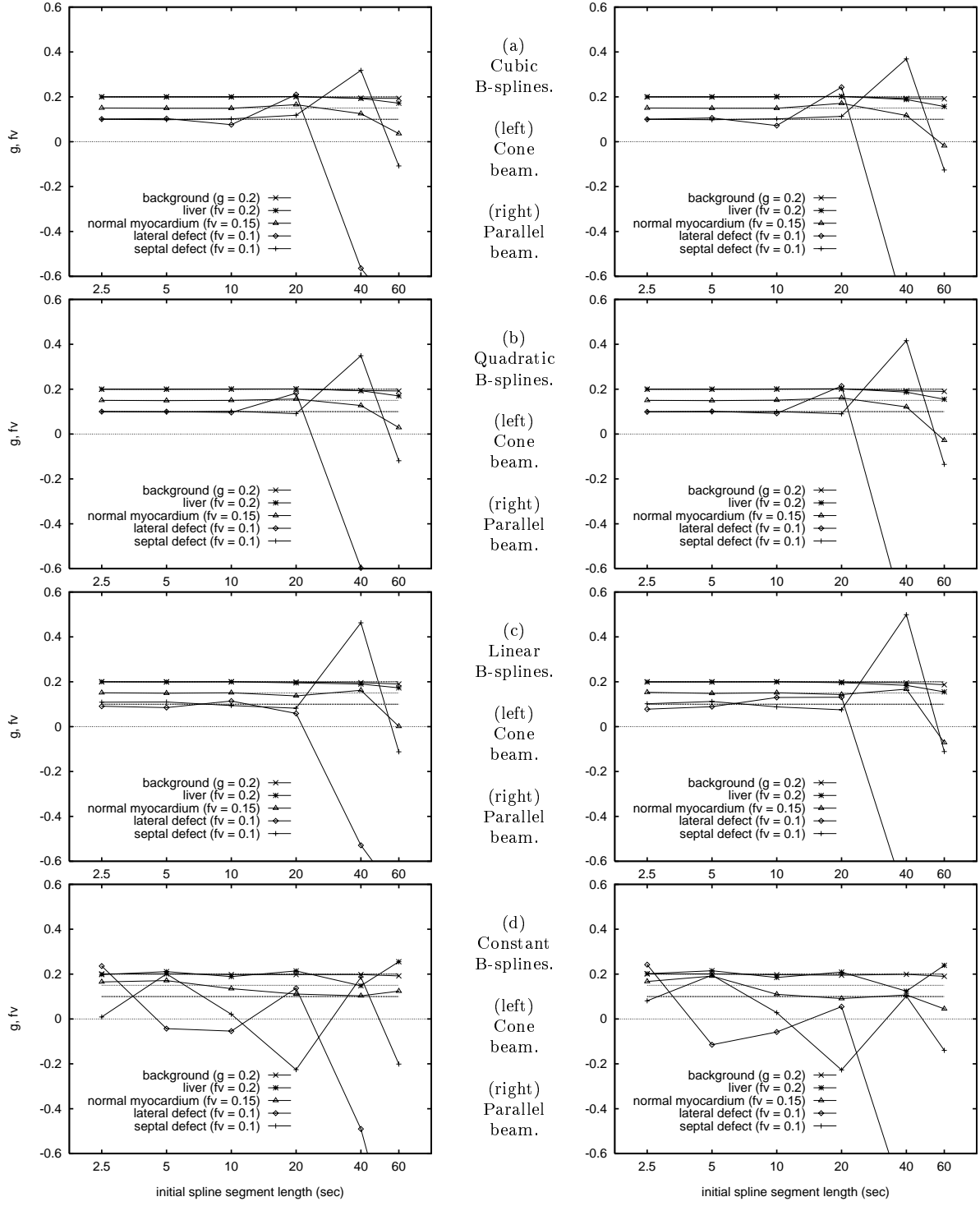


Figure 9: Background amplitude g and vascular fraction f_v^m parameters obtained from time-activity curves estimated directly from simulated noiseless cone beam (left) and parallel beam (right) projections, using piecewise cubic (a), quadratic (b), linear (c), and constant (d) B-spline temporal basis functions (Figure 5) and initial time segment lengths ranging between 2.5–60 sec. The amplitude g and fraction f_v^m are dimensionless. The simulated values are depicted by the dotted horizontal lines and listed in the figure legends. The biases are particularly small when using quadratic B-splines and initial time segment lengths of 2.5, 5, or 10 sec. The results for quadratic B-splines and an initial time segment length of 10 sec are listed in column (b) of Tables 1 and 2.

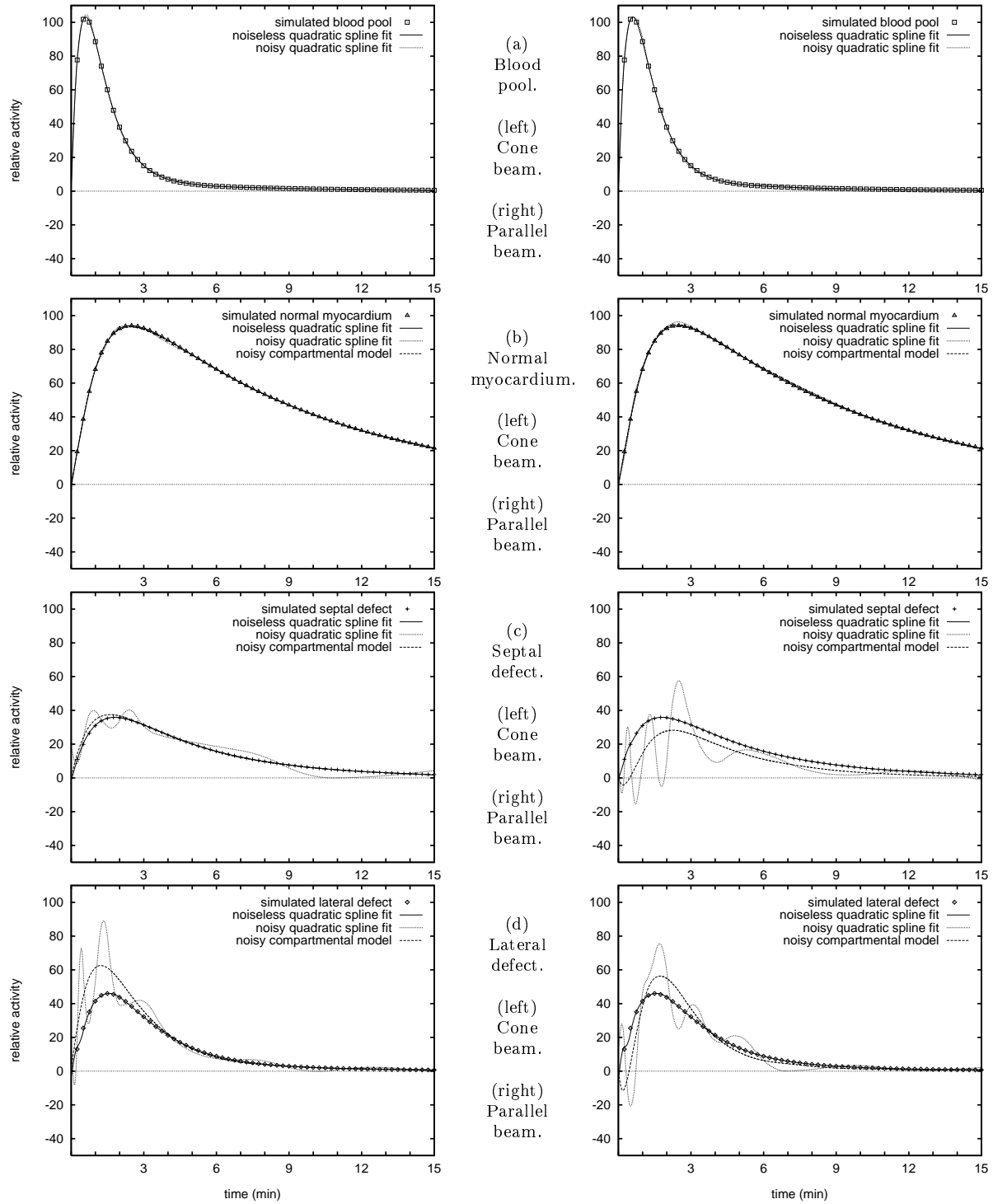


Figure 10: First of 100 noisy realizations: time-activity curves for (a) the blood pool, (b) the normal myocardium, (c) the septal defect, and (d) the lateral defect, estimated directly from simulated cone beam (left) and parallel beam (right) projections using temporal quadratic B-spline basis functions and an initial time segment length of 10 sec (Figure 5b). Samples of the simulated curves (Figure 4) are shown as points. The solid curves were estimated from noiseless projections, and the dotted curves were estimated from the first of 100 realizations of projections having Poisson noise. The dashed curves in (b), (c), and (d) are the one-compartment kinetic fits (Figure 2) to the noisy curves. The fitted kinetic model parameters are listed in column (c) of Tables 1 and 2.

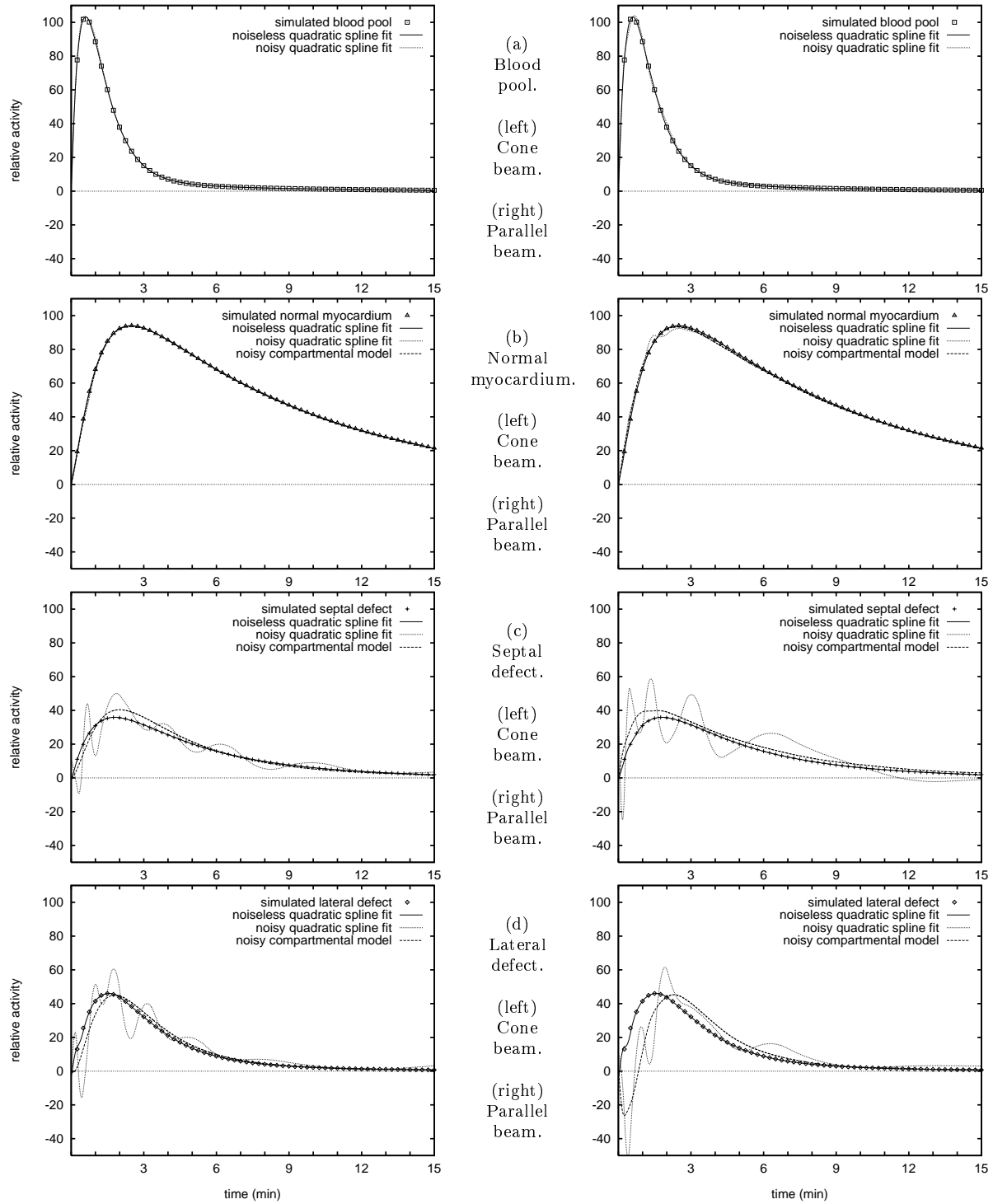


Figure 11: Second of 100 noisy realizations: time-activity curves for (a) the blood pool, (b) the normal myocardium, (c) the septal defect, and (d) the lateral defect, estimated directly from simulated cone beam (left) and parallel beam (right) projections using temporal quadratic B-spline basis functions and an initial time segment length of 10 sec (Figure 5b). Samples of the simulated curves (Figure 4) are shown as points. The solid curves were estimated from noiseless projections, and the dotted curves were estimated from the second of 100 realizations of projections having Poisson noise. The dashed curves in (b), (c), and (d) are the one-compartment kinetic fits (Figure 2) to the noisy curves. The fitted kinetic model parameters are listed in column (d) of Tables 1 and 2.

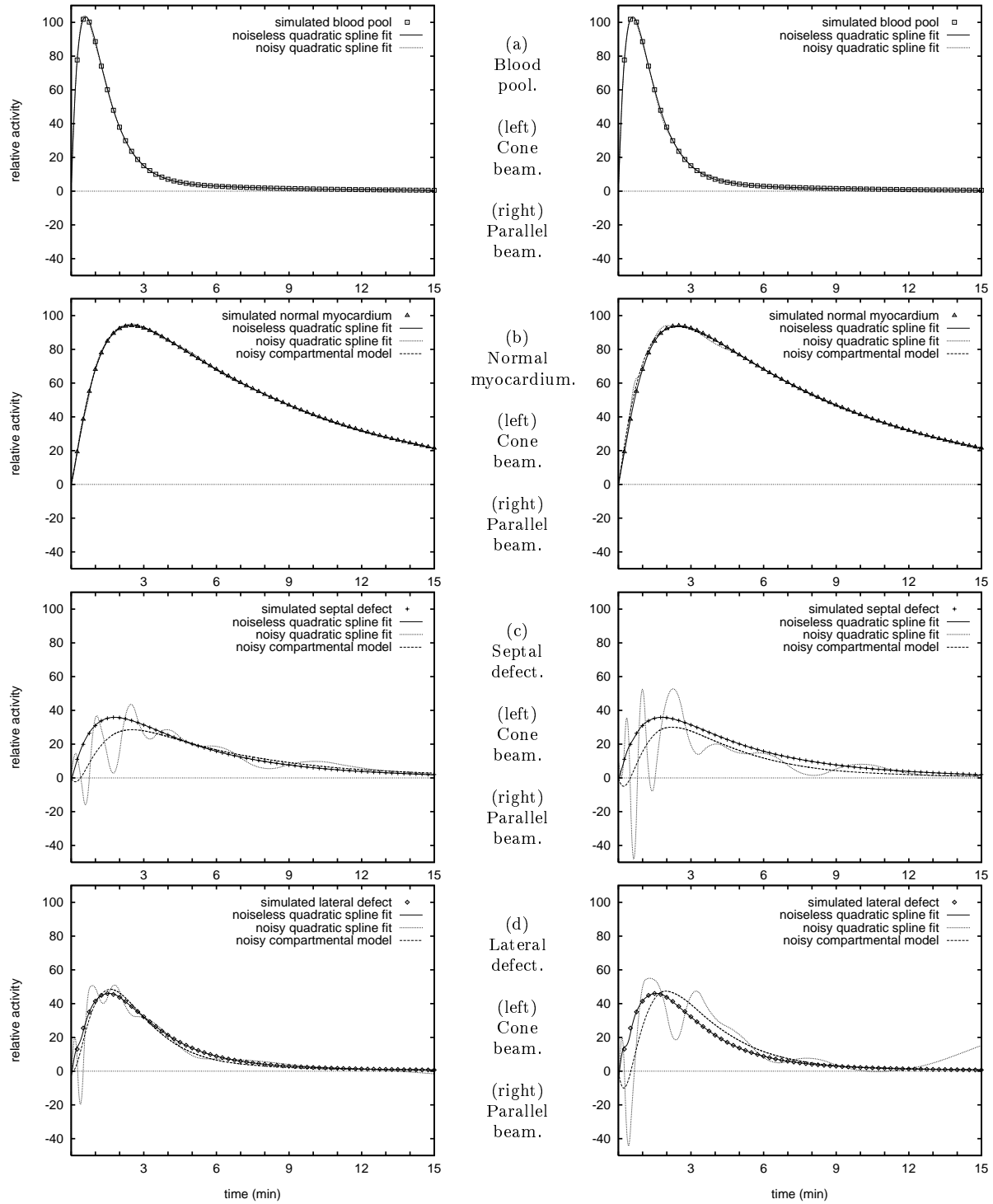


Figure 12: Third of 100 noisy realizations: time-activity curves for (a) the blood pool, (b) the normal myocardium, (c) the septal defect, and (d) the lateral defect, estimated directly from simulated cone beam (left) and parallel beam (right) projections using temporal quadratic B-spline basis functions and an initial time segment length of 10 sec (Figure 5b). Samples of the simulated curves (Figure 4) are shown as points. The solid curves were estimated from noiseless projections, and the dotted curves were estimated from the third of 100 realizations of projections having Poisson noise. The dashed curves in (b), (c), and (d) are the one-compartment kinetic fits (Figure 2) to the noisy curves. The fitted kinetic model parameters are listed in column (e) of Tables 1 and 2.